


Statistical Study on Multispacecraft Widespread Solar Energetic Particle Events During Solar Cycle 24

H. Xie^{1,2} , O. C. St. Cyr², P. Mäkelä^{1,2} , and N. Gopalswamy² 

¹Department of Physics, The Catholic University of America, Washington, DC, USA, ²NASA/Goddard Space Flight Center, Greenbelt, MD, USA

Key Points:

- Using a symmetric Gaussian fit, we find that the distribution width of SEPs increases with connection angle
- The average electron and proton release time delay relative to Type II onset is 14 and 32 min for strongly anisotropic events
- By including the true shock speed and true CME widths, we can improve the SEP intensity prediction and reduce RMS errors

Correspondence to:

H. Xie,
hong.xie@nasa.gov

Citation:

Xie, H., St. Cyr, O. C., Mäkelä, P., & Gopalswamy, N. (2019). Statistical study on multispacecraft widespread solar energetic particle events during solar cycle 24. *Journal of Geophysical Research: Space Physics*, 124, 6384–6402. <https://doi.org/10.1029/2019JA026832>

Received 12 APR 2019

Accepted 16 JUL 2019

Accepted article online 30 JUL 2019

Published online 13 AUG 2019

Abstract We conduct a statistical study on the large three-spacecraft widespread solar energetic particle (SEP) events. Longitudinal distributions of the peak intensities, onset delays, and relation between the SEP intensity, coronal mass ejection (CME) shock speed, width, and the kinetic energy of the CME have been investigated. We apply a Gaussian fit to obtain the SEP intensity I_0 and distribution width σ and a forward-modeling fit to determine the true shock speed and true CME width. We found a good correlation between σ and connection angle to the flare site and I_0 and the kinetic energy of the CME. By including the true shock speed and true CME widths, we reduce root-mean-square errors on the predicted SEP intensity by $\sim 41\%$ for protons compared to Richardson et al.'s (2014, <https://doi.org/10.1007/s11207-014-0524-8>) prediction. The improved correlation between the CME kinetic energy and SEP intensity provides strong evidence for the CME-shock acceleration theory of SEPs. In addition, we found that electron and proton release time delays (DT s) relative to Type II radio bursts increase with connection angles. The average electron (proton) DT is ~ 14 (32) min for strongly anisotropic events and ~ 2.5 (4.4) hr for weakly anisotropic events. Poor magnetic connectivity and large scattering effects are two main reasons to cause large delays.

1. Introduction

Recent observations of solar energetic particle (SEP) events from the Solar Terrestrial Relations Observatory (STEREO) A and B (STA and STB) (Kaiser et al., 2008) and near-Earth spacecraft at L1 have provided abundant evidence for wide longitudinal distributions of SEPs (e.g., Richardson et al., 2014; Rouillard et al., 2012; Wiedenbeck et al., 2013). Richardson et al. (2014) compiled a catalog of 209 individual >25 -MeV solar proton events in solar cycle 24 and found that 17% of these events were observed by all three spacecraft (i.e., 3-SC events) when the STEREO spacecraft were well separated by greater than 60° in heliolongitude from Earth. Several mechanisms have been proposed to explain such a large spread of SEP events. Coronal shocks driven by fast and wide coronal mass ejections (CMEs) are generally considered to be spatially extended particle sources that accelerate and inject particles into large regions in the heliosphere (Cliver et al., 1995). Cross-field transport in the corona and interplanetary (IP) space is another mechanism that results in widespread SEP events (Hu et al., 2017; Zhang et al., 2009; Zhang & Zhao, 2017). In addition, concurrence of multiple solar eruptions, large magnetic loops, and IP transient structures can also lead to widespread SEP events (e.g., Klein et al., 2008; Leske et al., 2012; Richardson et al., 1991; Schrijver et al., 2013).

In this paper, we investigate a set of 3-SC near-relativistic 62- to 105-keV electron events and 19- to 30-MeV proton events that show a wide longitudinal distribution of particles ($>90^\circ$). Our 3-SC events are selected from the large SEP events with intensity >10 pfu in the >10 -MeV energy channel of the Geostationary Operational Environmental Satellite system (GOES) and equivalent integrated channel of STEREO during solar cycle 24. We extend the Richardson et al.'s (2014) 3-SC event list by adding true shock speeds, true CME angular widths, and electron anisotropies. We focus on studying the longitudinal variation of the electron and proton intensities, onset delays, time profiles, and the relation between SEP intensities and true CME shock properties. In Richardson et al. (2014), there are two aspects that can be improved. First, the CME speeds used in their study are sky-plane speeds from Coordinate Data Analysis Workshop (CDAW) CME catalog (Yashiro et al., 2004; <http://cdaw.gsfc.nasa.gov/CMElist/>) instead of the CME shock true speeds. Second, the effect of CME widths on the SEP intensity was not included due to the lack of measurements of true CME width. The CME shock true speeds and CME widths can only be obtained by three-dimensional (3-D)

CME reconstruction methods. In this study we apply a forward modeling with a flux rope (FR) model plus an oblate spheroid shock model to fit 3-D CME shocks. Using combined STEREO, *Solar and Heliospheric Observatory* (SOHO) and *Solar Dynamics Observatory* (SDO) white light (WL) and extreme ultraviolet (EUV) observations as constraints, we are able to determine the true radial speed of the shock and CME angular widths. By conducting correlation analyses between the SEP intensity, shock speed, CME width, and kinetic energy, we demonstrate how including CME angular widths can improve the SEP prediction and reduce the correlation scattering. In addition, we study the electron anisotropies that are observed at different spacecraft and conduct analyses on the electron and proton release time delays with respect to Type II onset times. We compare the SEP release delays for strongly anisotropic events with weakly anisotropic events to examine the various mechanisms (direction injection vs. transport diffusion) that might be responsible for the wide longitudinal SEP events.

The paper is organized as follows. In section 2, we give an overview of observations of electron and proton intensities, solar observations, and event selection. In section 3, we study the longitudinal dependence of electron and proton peak intensities and the Gaussian width's dependence on connection angle (CA) to the flare site. Section 4 describes how SEP onset delays vary as a function of CA. In section 5, we introduce the forward modeling method and show the CME shock fit results and present the SEP prediction formula. Finally, sections 6 and 7 are discussion and summary of the study, respectively.

2. Observations and Event Selection

The electron observations used in this study are from the Solar Electron and Proton Telescope (Müller-Mellin et al., 2008) on the STEREO spacecraft and the Electron Proton and Alpha Monitor (EPAM; Gold et al., 1998) on the *Advanced Composition Explorer* (ACE). The proton observations are from the High Energy Telescope (HET; von Rosenvinge et al., 2008) on the STEREO spacecraft and the Energetic Particles: Acceleration, Composition and Transport (EPACT) on the Wind spacecraft (Gold et al., 1998). For electrons, we used intensities at 65–105 keV from the STEREO/Solar Electron and Proton Telescopes and at 62–103 keV from ACE/EPAM. For protons, we examined energy ranges from 21 to 30 MeV which made of the combination of HET 20.8- to 23.8-, 23.8- to 26.4-, and 26.3- to 29.7-MeV energy channels, to match the similar energy channel 19–28 MeV of Wind/EPACT. Note that in this study we used Wind/EPACT proton data instead of the Energetic and Relativistic Nuclei and Electron instrument (ERNE; Torsti et al., 1995) data on the SOHO spacecraft because SOHO flips every 3 months, the ERNE viewing direction relative to the nominal IP magnetic field (IMF) changing from being along to perpendicular to the IP magnetic field and affecting the observed intensity.

We study the large SEP events with intensity >10 pfu in the >10 -MeV energy channel of GOES and equivalent integrated channel of STEREO/HET from January 2010 to April 2014, when the longitudinal separation of each of STEREOs exceeded $\sim 60^\circ$ from Earth. Twenty eight 3-SC SEP events are selected in this study, which is based on the criterion that at least one spacecraft must have a CA greater than 90° . Here CA is defined as the longitudinal separation angle between the flare site and the magnetic footpoint of the observing spacecraft. Positive CA denotes a flare source located at the western side of the spacecraft magnetic footpoint; negative CA represents a source to the east. We have excluded the events when their peak intensities on any of the three spacecraft have been interfered by either preceding events or ion contamination or the peak increases are too small to be determined. The flare locations were identified using EUV images and movies taken by the EUV Imager (Howard et al., 2008; Wuelser et al., 2004) on the STEREO spacecraft and by the Atmospheric Imaging Assembly (Lemen et al., 2012) on the SDO spacecraft. The longitudes of the spacecraft magnetic footpoints were calculated assuming a Parker spiral and taking into account the measured solar wind speed during the event onset. Similar to Xie et al. (2016), we use the intersection slope method to determine the SEP onset times observed in situ at 1 AU from 10-min average data. The electron and proton solar particle release (SPR) time is then computed by shifting the onset time of SEPs by the particle traveling time along the nominal path length of 1.25 AU, which is computed assuming an average solar wind speed of 320 km/s. A correction of ~ 8.3 min of the light travel time has been added to the SPR times so that they can be directly compared to radio emission onset times observed at 1 AU.

In Table 1, Columns 1 to 4 list the event number, date, Type III radio burst onset times, and flare locations. We consider the Type III onset as the expected solar eruption times instead of the flare onset time. Columns 5 to 10 list the CAs and anisotropy values for each spacecraft, and Columns 11 to 13 list the forward-modeling

Table 1

Event Number, Date, Type III Radio Burst Onset Time, Flare Location, CA, A Value, and Coronal Mass Ejection Shock Fit Results

#	Date	T-III onset (UT)	Flare loc	Connection angle			Anisotropy			GCS + shock fit		
				STB	L1 (°)	STA	STB	L1	STA	v_{shock} (km/s)	κ	α (°)
1	2010/08/14	09:56	N17W52	53	-2	-96	1.82	0.79	0.07	1,139	0.40	23
2	2011/08/04	03:52	N19W36	77	-36	-131	-0.03	1.40	0.09	2,068	0.52	35
3	2011/08/09	08:02	N17W69	100	27	-77	-0.53	1.11	0.11	1,694	0.40	35
4	2011/09/22	10:40	N09E89	-32	-139	114	1.55	0.54	0.54	1,916	0.72	42
5	2011/11/03	22:17	N09E154	-127	138	12	-2.70	1.51	2.17	1,140	0.75	53
6	2011/11/26	07:10	N17W49	92	-11	-113	0.53	1.49	0.34	987	0.36	37
7	2012/01/23	03:42	N28W21	64	-33	-152	0.12	0.37	0.19	2,014	0.67	57
8	2012/01/27	18:16	N27W71	129	23	-98	0.16	0.25	0.14	2,475	0.51	51
9	2012/03/04	11:02	N19E61	-23	-125	127	0.87	0.53	0.15	1,405	0.55	20
10	2012/03/24	00:10	N18E164	-118	123	22	-0.17	0.21	1.01	1,991	0.73	20
11	2012/05/17	01:32	N11W76	119	8	-78	0.44	2.04	0.25	1,579	0.51	42
12	2012/07/06	23:04	S13W59	108	-2	-120	0.53	0.96	0.13	1,528	0.43	23
13	2012/07/12	16:31	S15W01	43	-65	-176	-1.24	1.84	0.13	1,398	0.64	22
14	2012/07/17	14:01	S28W75	120	14	-126	0.22	0.66	0.06	1,122	0.48	27
15	2012/08/31	19:45	S25E59	-1	-119	140	2.72	0.58	0.26	1,485	0.77	57
16	2012/11/08	10:40	S14W160	-155	110	-22	-0.55	0.81	2.25	1,370	0.55	29
17	2013/03/05	03:18	N10E144	-90	157	14	0.54	0.48	3.34	1,558	0.86	54
18	2013/04/11	07:03	N09E12	57	-77	-167	2.11	0.81	0.40	1,097	0.93	53
19	2013/05/22	13:10	N15W70	153	15	-133	-0.15	0.71	0.08	1,567	0.84	64
20	2013/06/21	02:51	S16E73	22	-123	90	1.00	0.11	0.14	2,129	0.56	41
21	2013/08/19	22:56	N12W178	-124	117	-32	-0.33	0.15	0.25	1,114	0.67	78
22	2013/09/29	21:57	N17W29	72	-65	-151	0.16	0.96	0.32	1,544	0.63	74
23	2013/10/25	15:02	S06E69	-13	-147	97	0.59	0.41	0.17	1,266	0.34	44
24	2013/12/26	03:05	S09E166	-70	139	-12	1.47	0.60	1.34	1,535	0.50	22
25	2014/01/06	07:46	S15W112	-168	40	-118	-0.28	0.76	0.80	1,386	0.25	32
26	2014/01/07	18:04	S15W11	117	-20	-175	0.39	0.53	0.56	2,299	0.65	42
27	2014/02/25	00:46	S12E82	43	-131	65	0.00	0.41	0.95	2,289	0.64	44
28	2014/04/02	13:25	N11E53	36	-112	-105	1.15	0.20	0.18	1,500	0.67	31

Note. v_{shock} is the CME shock true speed, and κ and α are flux rope aspect ratio and half-width (see section 5). STA and STB = Solar Terrestrial Relations Observatory A and B.

fit results (section 5). The Type III onset times are measured to ± 5 -min accuracy at ~ 14 MHz by using STEREO/WAVES (Bougeret et al., 2008) and WIND/WAVES (Bougeret et al., 1995) radio data (<http://cdaw.gsfc.nasa.gov/images/stereo/swaves/> and <http://cdaw.gsfc.nasa.gov/images/wind/waves/>).

3. Longitudinal Dependence of SEP Intensity

To investigate the longitudinal dependence of SEP intensity, we fit the longitudinal distribution of electron and proton peak intensities with Gaussian function:

$$I(\phi) = I_0 \exp[-(\phi - \phi_0)^2 / 2\sigma^2], \quad (1)$$

where I_0 is the peak intensity at the Gaussian center, σ is the standard deviation or width, ϕ is the CA, and ϕ_0 is the center of the Gaussian. Figures 1a and 1b show the peak intensities of electrons and protons detected by each spacecraft as function of CAs. Different symbols mark different spacecraft, and each color denotes an individual 3-SC event. The electron and proton peak intensities used in the Gaussian fit are background-corrected peak values within 48 hr from onset times of the associated Type III radio burst, and the associated local IP shock peaks have been excluded. We have also excluded ambiguous events with poor

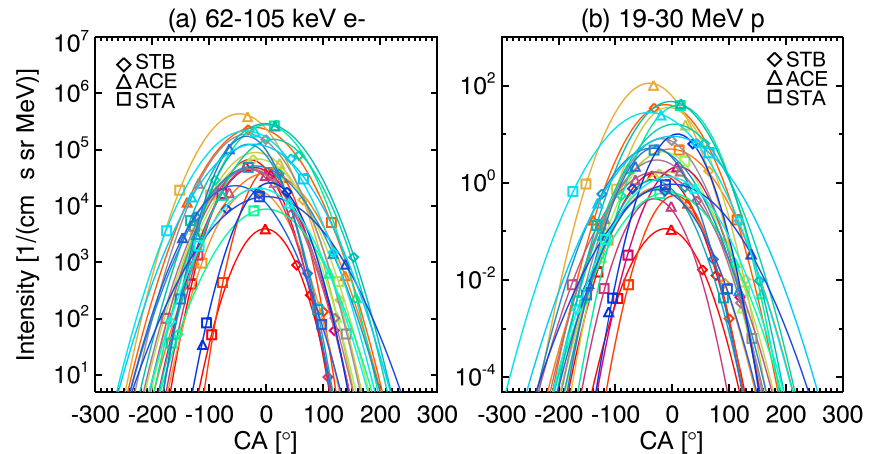


Figure 1. Peak intensities as a function of CA for (a) 62- to 105-keV electrons and (b) 19- to 30-MeV protons. Positive (negative) CAs denote a source westward (eastward) to the spacecraft magnetic footprint. Different symbol marks different spacecraft and each color denotes a three-spacecraft event. STA and STB = Solar Terrestrial Relations Observatory A and B; ACE = Advanced Composition Explorer; CA = connection angle.

fit with $|\phi_0| > 90^\circ$. An intercalibration factor of 1/1.4 (1/1.5) has been applied to the ACE (Wind) data to correct the different instrument responses after we compare the ACE/EPAM and Wind/EPACT data with the STEREO measurements. Table 2 lists the Gaussian peak intensity I_0 and peak intensities of electrons and protons observations from the STA, STB, and ACE/Wind spacecraft.

Figure 2 shows distributions of Gaussian width σ and Gaussian center ϕ_0 for electrons (top panels) and protons (bottom panels). A wide range of σ 27–59° was found with a mean of 42° for electrons and 28–54° with a mean of 39° for protons. The Gaussian center tends to occur around zero CA with an average offset of approximately $-18^\circ \pm 17^\circ$ for electrons and approximately $-15^\circ \pm 16^\circ$ for protons. Large standard deviations in the ϕ_0 distribution indicate that asymmetries, that is, shifts of the Gaussian center, to both east and west existed, as shown in Figures 2b and 2d.

To further investigate the Gaussian width of the CA distribution of the SEP peak intensities, we applied a symmetric Gaussian fit centered on $\phi_0 = 0$ to the 3-SC events, that is, the Gaussian peak is setup at zero CA. For each 3-SC event, we perform the symmetric Gaussian fit over western and eastern events separately by pairing a western event ($CA > 50^\circ$) or an eastern event ($CA < -50^\circ$) with its best-connected event ($|CA| < 30^\circ$). Figure 3 shows the symmetric Gaussian fit results. We can see that the average width of eastern events is greater than that of western events. For electrons, the mean width of eastern events is 47°, and that of the western events is 35°. For protons, the mean width of eastern events is 42° and western events is 32°. Furthermore, we find a good correlation between σ and CA. The correlation coefficients are 0.75 (–0.62) and 0.74 (–0.69) for western (eastern) electron and proton events, respectively. For electrons, the widths of western and eastern events over the CA ϕ vary as $\sigma_{\text{west}} = 7.1 + 0.26\phi$ and $\sigma_{\text{east}} = 12.9 - 0.28\phi$; for protons, $\sigma_{\text{west}} = 8.4 + 0.21\phi$ and $\sigma_{\text{east}} = 7.9 - 0.28\phi$.

Note that using nominal Parker spiral field line to estimate the magnetic footprint may result in an uncertainty of $\sim 20\text{--}30^\circ$ (Xie et al., 2016). Lario et al. (2017) showed that discrepancy between the estimates from the Parker spiral field line and the potential field source surface model and other magnetohydrodynamic models can be as large as $\pm 20^\circ$. They indicated that the footprint locations are not only model dependent but also rely on the magnetogram input data used to compute the low coronal magnetic fields below 2.5–30 R_s depending on the specific model. The ambiguous determination of the magnetic footprint locations is the major cause for the large scatter in Figure 3. However, since no systematic shifts were found between the estimates from the Parker spiral field line and potential field source surface and other models (Lario et al., 2017), the correlation coefficient and the linear fit relation between CA and theta would not be significantly affected, as shown in Figure 3.

4. Electron and Proton Release Times With Respect to Type II Onset Times

It is generally believed that Type III radio bursts are associated with flare-accelerated electrons, while Type II radio bursts are produced by electrons accelerated by CME-driven shocks. In this section, we compare

Table 2
Gaussian Peak Intensity and Observed Peak Intensities of Electrons and Protons

#	Date	1/(cm ² s sr MeV)							
		Electron peak intensity				Proton peak intensity			
		Gaussian	STB	L1	STA	Gaussian	STB	L1	STA
1	2010/08/14	4.14e+03	8.92e+02	4.13e+03	5.16e+01	1.14e−01	1.63e−02	1.10e−01	4.16e−03
2	2011/08/04	6.99e+04	2.61e+02	5.39e+04	4.10e+02	1.65e+00	1.24e−02	1.42e+00	1.46e−02
3	2011/08/09	5.03e+04	1.32e+02	3.37e+04	4.38e+02	5.52e−01	1.61e−03	3.82e−01	8.00e−03
4	2011/09/22	2.61e+05	2.29e+05	1.23e+04	5.09e+03	4.09e+01	3.47e+01	1.72e−01	1.73e−01
5	2011/11/03	4.08e+04	9.26e+02	6.06e+02	3.80e+04	4.97e+00	1.12e−01	3.45e−02	4.73e+00
6	2011/11/26	2.09e+04	1.63e+02	2.01e+04	9.66e+02	8.09e−01	8.68e−03	7.50e−01	6.63e−02
7	2012/01/23	4.58e+05	1.28e+04	4.06e+05	1.91e+04	1.13e+02	1.76e+00	1.02e+02	9.47e−01
8	2012/01/27	9.40e+04	2.13e+02	6.01e+04	1.57e+04	3.58e+01	1.03e−02	1.55e+01	7.43e−01
9	2012/03/04	7.21e+04	6.73e+04	4.05e+03	4.57e+02	1.69e+00	1.55e+00	2.89e−02	5.92e−03
10	2012/03/24	4.92e+04	3.45e+03	1.12e+02	2.67e+04	4.36e+00	9.05e−02	2.65e−03	2.81e+00
11	2012/05/17	5.08e+04	6.13e+01	3.89e+04	1.67e+03	2.15e+00	4.42e−03	2.14e+00	3.25e−02
12	2012/07/06	4.79e+04	9.12e+00	3.64e+04	1.34e+03	4.71e−01	1.18e−05	3.30e−01	6.68e−03
13	2012/07/12	4.86e+04	7.07e+03	1.81e+04	1.01e+02	1.67e+00	4.28e−01	1.16e+00	8.00e−03
14	2012/07/17	4.81e+04	1.02e+02	2.77e+04	4.36e+03	2.96e+00	3.39e−03	1.75e+00	1.40e−01
15	2012/08/31	2.00e+05	1.52e+05	2.65e+04	5.32e+01	8.14e+00	7.44e+00	1.84e−01	6.26e−04
16	2012/11/08	9.25e+03	5.28e+01	6.74e+02	8.19e+03	6.38e−01	3.72e−03	2.30e−02	6.03e−01
17	2013/03/05	2.91e+05	2.88e+04	2.49e+02	2.64e+05	3.98e+01	5.44e−01	5.18e−03	3.91e+01
18	2013/04/11	1.61e+05	7.91e+04	1.62e+04	3.67e+01	1.62e+01	6.45e+00	2.00e+00	3.72e−03
19	2013/05/22	3.05e+05	1.23e+03	2.79e+05	5.52e+03	4.74e+01	9.71e−03	4.30e+01	1.33e−01
20	2013/06/21	1.31e+05	3.73e+04	3.26e+03	1.45e+02	1.14e+00	8.14e−01	8.31e−02	4.28e−03
21	2013/08/19	5.41e+04	6.50e+03	1.50e+03	4.86e+04	5.18e+00	5.90e−01	6.04e−03	4.74e+00
22	2013/09/29	1.83e+05	6.36e+02	1.09e+05	2.23e+02	5.25e+00	2.68e−02	2.20e+00	4.92e−03
23	2013/10/25	2.41e+04	1.63e+04	2.87e+03	7.84e+01	7.22e−01	6.77e−01	8.45e−03	6.58e−03
24	2013/12/26	1.54e+04	8.87e+03	9.72e+02	1.46e+04	9.41e−01	7.62e−01	3.43e−02	9.15e−01
25	2014/01/06	2.18e+04	8.83e+01	1.18e+04	1.95e+03	1.33e+00	2.45e−03	7.77e−01	6.89e−02
26	2014/01/07	2.27e+05	1.50e+03	2.17e+05	3.63e+03	2.81e+01	1.66e−01	2.50e+01	6.68e−01
27	2014/02/25	1.31e+05	6.89e+04	1.52e+04	3.03e+04	9.14e+00	6.50e+00	3.85e−01	4.16e+00
28	2014/04/02	2.72e+04	1.77e+04	3.63e+01	8.39e+01	1.01e+01	6.36e+00	2.22e−03	4.24e−03

Note. The peak intensities at Advanced Composition Explorer and Wind have been corrected by intercalibration factors of 1/1.4 and 1/1.5. STA and STB = Solar Terrestrial Relations Observatory A and B.

electron and proton release times with Type II radio burst onset times. Table 3 lists electron and proton release times and onset times of the associated Type II radio bursts. Columns 1 to 4 are event number, date, metric, and deca-hectometric (DH) Type II onset times. The metric Type II onset times are compiled by the CDAW Data Center at Goddard Space Flight Center (<https://cdaw.gsfc.nasa.gov/CME&urlscore;list/NOAA/org&urlscore;events&urlscore;text/>). When observations of the metric Type II bursts are not available, the DH Type II onset times are used instead, as measured to ±10-min accuracy by WAVES radio experiments on the STEREO and Wind spacecraft. Columns 4 to 6 list the 62- to 105-keV electron release times at three spacecraft, and Columns 7 to 9 are the 19- to 30-MeV proton release times at three spacecraft, where the electron and proton release times for weakly anisotropic events are nominal values since they are computed by neglecting scattering effects (see section 4.1).

4.1. Electron Release Times With Respect to Type II Onset Times

Figure 4 shows 62- to 105-keV electron release time delays (DTs) relative to Type II onset times for strongly anisotropic events ($A \geq 0.6$; Figure 4a) and for weakly anisotropic events ($A < 0.6$; Figure 4b) as function

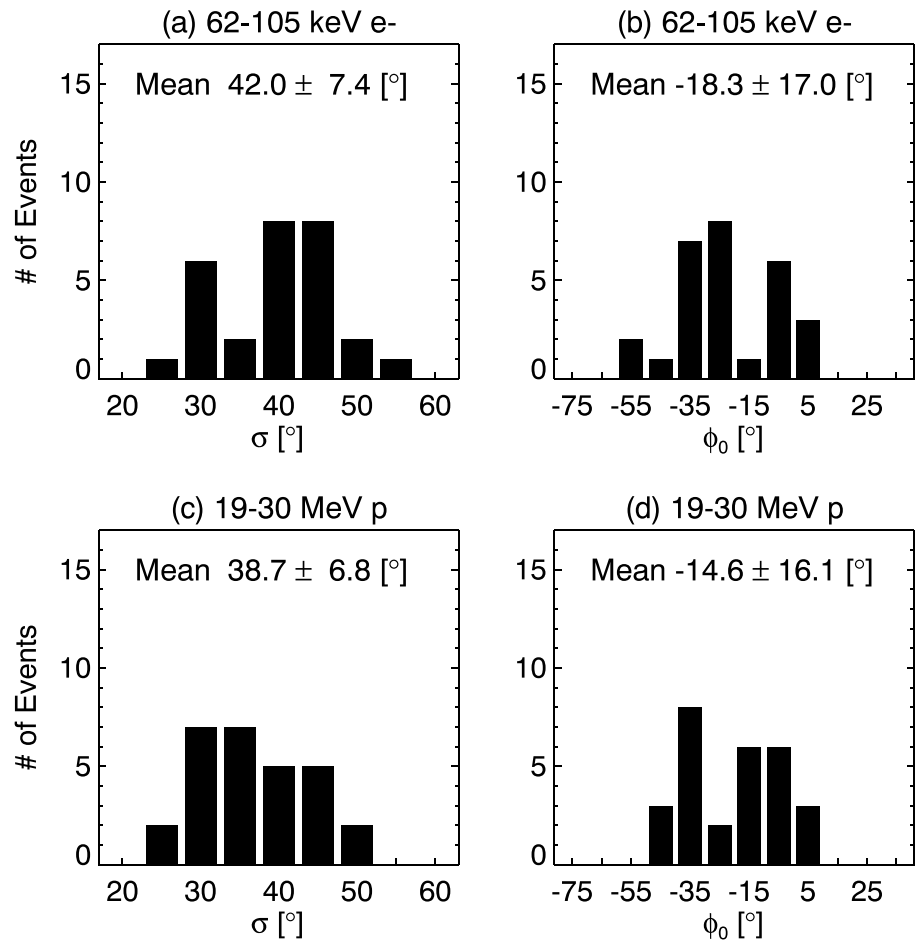


Figure 2. Distributions of Gaussian width σ and Gaussian center ϕ_0 in asymmetric Gaussian fit for (a and b) 62- to 105-keV electrons and (c and d) 19- to 30-MeV protons, respectively.

of $|CA|$. Here the anisotropy value (A value) is defined as

$$A = \frac{3 \int_{-1}^{+1} I(\mu) \cdot \mu \cdot d\mu}{\int_{-1}^{+1} I(\mu) \cdot d\mu}, \quad (2)$$

where $I(\mu)$ is the intensity at a given pitch-angle direction and μ is the pitch angle cosine (see details in Xie et al., 2017). In Figure 4a, we can see a good correlation between DT and $|CA|$ with a correlation coefficient of 0.70. The linear fit yields $DT = -0.7 + 0.29|CA|$ in minutes, indicating that the electron SPR delay increases ~ 29 min/ 100° of $|CA|$. The histogram of the SPR delays shows that the SPR delays range from -25 to 54 min with a mean value of 13.5 min (Figure 4d). The good correlation between DT and $|CA|$ indicates that the larger the $|CA|$ is, the longer traveling time is needed for the expanding shock to reach at Connecting with the OBserver point. The scatter around the best-fit line suggests that the shock expanding times vary drastically event by event. In Figure 4a, the majority of the events are within ± 15 min of the best-fit line, that is, the area delimited by the two dashed lines, except the four events labeled with an event number and spacecraft letter (22-E, 20-B, 28-B, 5-E), where A, B, and E denote STA, STB, and near-Earth. Two outliers (28-B and 5-E) are on the margin of the dashed lines; however, 22-E and 20-B are largely deviated from the best-fit line with DT s of 41 and -25 min, respectively (see detailed discussion in section 6).

Figure 4b plots the electron release time delays for weakly anisotropic events $A < 0.6$. While the SEPs with strong anisotropy can be assumed to propagate nearly scatter-free, the particles in weakly anisotropic events may have experienced both parallel and perpendicular diffusion before reaching the spacecraft. The scattering effects play important roles in weakly anisotropic events and cause large onset delays. Similar to Figure 4a, in Figure 4b, we find a good correlation between DT and $|CA|$ with correlation coefficient of ~ 0.69 .

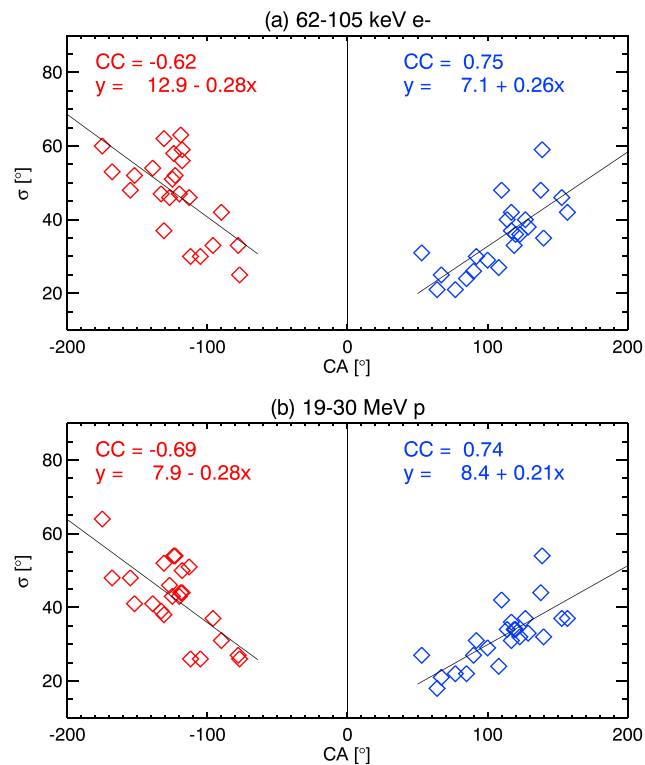


Figure 3. Gaussian width σ as a function of CA in the symmetric Gaussian fit for western events (blue) and eastern events (red) for (a) 62- to 105-keV electrons and (b) 19- to 30-MeV protons, respectively. CA = connection angle.

However, DT s in Figure 4b are much larger than Figure 4a, which range from ~ 0.7 to 7.4 hr with a mean of ~ 2.5 hr (Figure 4d). The linear fit gives $DT = -2.8 + 0.05|CA|$ in hours, and DT increases ~ 5 hr/ 100° of $|CA|$. Most of the events are within ± 2 hr of the best-fit line except three outliers: two events above and one below the dashed lines. The two outliers above the dashed lines 9-A and 25-B are small SEP events with high background-to-peak ratios, which, on one hand, their real onset times are disguised by the elevated background and, on the other hand, the small intensity events tend to have a slow rising profile and experience large scattering effect before their intensities reach the detectable flux levels.

In Figure 4c, we plot the events with $A \geq 0.6$ (blue) and with $A < 0.6$ (red) together. The slopes of the regression lines of the two groups are evidently different. The detailed linear fits to the data are shown in Figures 4a and 4b. Note that the y axis is in units of minutes in Figure 4a and hours in Figure 4b. The correlation between the electron delay and CA in Figures 4a and 4b is caused by different processes. For the strongly anisotropic events, the particles are accelerated by the CME-driven shock and released on each field line when the shock crosses near the Sun; therefore, the SEP-Type II delay is proportional to the time for the shock to expand from the flare site to the magnetic connection point of each spacecraft. For the weakly anisotropic events, the wide spread of SEPs results from cross-field diffusive transport processes in the IP medium, and the particle delay time is determined by the perpendicular diffusion coefficients as well as the ambient magnetic turbulence level. In Figure 4c, there is a transition region where the two groups are overlapping and the events in this region have an anisotropy close to ~ 0.6 and delays of ~ 60 – 90 min. It is possible that both the extended shock and perpendicular diffusion near the Sun and in the IP medium affect the marginal events in this region (e.g., Dresing et al., 2014). Otherwise, most weakly anisotropic events with $A < 0.4$ have delays larger than 1.5 hr, and the most strongly anisotropic events with $A > 0.6$ have delays less than 48 min.

4.2. Proton Release Time Delays Versus Electron Release Time Delays

Figure 5 compares the 62- to 105-keV electron SPR time delays DT_e with the 19- to 30-MeV proton SPR time delays DT_p relative to Type II onset times for strongly anisotropic events ($A \geq 0.6$; Figure 5a) and for weakly anisotropic events ($A < 0.6$; Figure 5b). Red diamonds in the figure denote the pair (DT_e, DT_p) . The dotted line represents where DT_p is equal to DT_e , and the solid line is the linear fit. In the figure, we can see that

Table 3
Electrons and Protons Release Times and Type II Radio Burst Onset Times

#	Date	mTypeII	DH-TypeII	Electron release time			Proton release time		
		onset (UT)	onset (UT)	(UT)			(UT)		
				STB	L1	STA	STB	L1	STA
1	2010/08/14	09:52	—	10:05	09:59	11:00	10:29	10:12	12:39
2	2011/08/04	03:54	04:12	05:03	04:05	06:44	06:52	04:22	11:30
3	2011/08/09	08:01	08:20	IC	08:02	AM	NA	08:02	NA
4	2011/09/22	10:39	11:00	10:43	12:36	NA	10:52	13:16	DG
5	2011/11/03	DG	22:30 ^a	23:01	22:49	22:25	23:17	23:15	22:41
6	2011/11/26	—	07:15	08:13	07:13	IC	08:20	07:34	13:00
7	2012/01/23	—	04:00	AM	AM	06:26	05:33	04:10	06:43
8	2012/01/27	18:10	18:30	AM	AM	19:53	NA	AM	20:45
9	2012/03/04	—	11:12	NA	12:33	17:05	13:40	16:20	NA
10	2012/03/24	DG	00:20 ^a	02:22	NA	00:19	02:54	NA	00:28
11	2012/05/17	01:31	01:42	03:10	01:33	03:49	05:32	01:34	05:31
12	2012/07/06	23:09	23:14	NA	NA	01:30 ^b	NA	23:30	03:24 ^b
13	2012/07/12	16:25	16:45	16:36	16:41	NA	16:59	16:48	NA
14	2012/07/17	—	14:40	NA	14:39	18:48	NA	14:59	NA
15	2012/08/31	19:42	20:00	19:54	20:51	NA	20:02	21:56	06:03
16	2012/11/08	DG	10:50 ^c	NA	11:01	10:44	NA	11:20	10:49
17	2013/03/05	DG	03:35 ^c	04:31	08:05	03:24	06:10	13:56	03:36
18	2013/04/11	07:02	07:12	07:09	07:36	12:03	07:18	07:43	13:02
19	2013/05/22	12:59	13:10	NA	13:17	17:43	23:29	13:30	19:04
20	2013/06/21	—	03:31	03:06	07:07	04:12	03:41	09:07	09:30
21	2013/08/19	DG	22:57 ^c	02:26 ^b	03:26 ^b	NA	04:07 ^b	05:06 ^b	00:26 ^b
22	2013/09/29	—	21:53	23:22	22:40	NA	01:04	23:19	07:08
23	2013/10/25	14:58	15:08	NA	18:45	16:27	16:15	19:03	17:41
24	2013/12/26	DG	03:05 ^a	03:30	03:59	03:20	03:45	04:56	03:58
25	2014/01/06	07:45	07:57	15:07	07:54	08:31	17:46	07:55	09:16
26	2014/01/07	18:17	18:33	20:28	NA	IC	22:14	19:15	AM
27	2014/02/25	00:50	01:02	IC	02:04	00:56	01:00	03:35	00:59
28	2014/04/02	13:23	13:42	13:55	NA	14:35	14:41	NA	15:53

Note. NA = the increase is too weak to be identified; IC = ion contamination; AM = ambiguous increase may not associated with the event or high background; DH = deca-hectometric; STA and STB = Solar Terrestrial Relations Observatory A and B.

^aDH Type II onset times from STB WAVES. ^bOccurred on the next day. ^cDH Type II onset times from STA WAVES.

DT_e is well correlated with DT_p in both Figures 5a and 5b, with correlation coefficients of 0.90 for strongly anisotropic events and 0.78 for weakly anisotropic events. The proton delays DT_p in (Figure 5a) ranges from ~1 to 111 min with a mean value of ~32 min and 1.1–10.4 hr with a mean value of ~4.4 hr. Overall, DT_p is greater than DT_e by ~0–57 min for strongly anisotropic events, and the average delay $DT_p - DT_e$ is ~18 min. For weakly anisotropic events, DT_p is greater than DT_e by ~0.1–5.9 hr, and the average delay is ~1.9 hr. The linear fit in Figure 5a gives $DT_p = 12.4 + 1.45DT_e$ in minutes and $DT_p = 1.6 + 1.08DT_e$ in hours in Figure 5b. In Figure 5c, we plot the events with $A \geq 0.6$ (blue) and with $A < 0.6$ (red) together. It is shown that the slopes in the two groups are similar. The proton delay DT_p correlates with DT_e , and there is no significant change in the slope of the regression line of the two groups, although the delays between DT_p and DT_e in the two groups are caused by different processes. In the first case, the proton delay relative to electrons is due to longer times needed to accelerate protons to the detectable flux level. In the latter case, the delay $DT_p - DT_e$ results from the diffusive transport processes, where the protons are more easily trapped in the magnetic turbulence and making it harder for protons to escape from the upstream into the IP medium (e.g., Lario et al., 2017). Similar to the electron events, the proton events with large delays are small intensity events

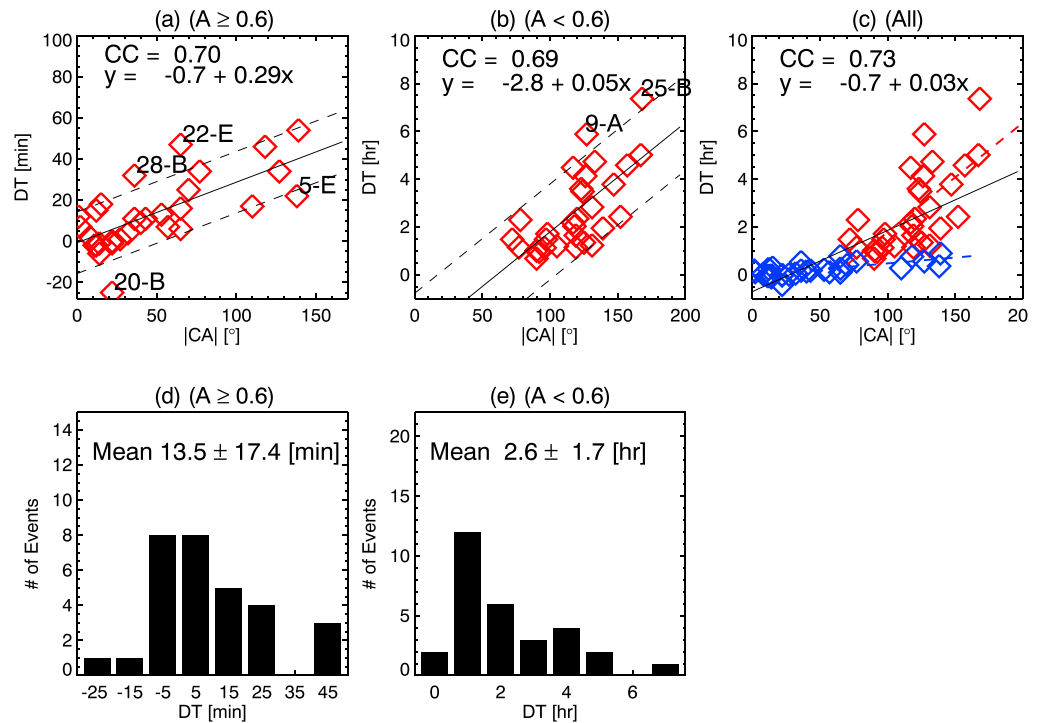


Figure 4. Delays of electron release times relative to Type II onset times DT as a function of $|CA|$ for (a) strongly anisotropic events, (b) weakly anisotropic events, and (c) for all the events, where blue and red diamonds denote strongly and weakly anisotropic events, respectively. (d) and (e) are histograms of DT for strongly and weakly anisotropic events, respectively. The dashed lines delimit areas (a) within 15 min and (b) 2 hr of the best-fit lines. The individual events labeled with an event number and spacecraft letter are outliers. CA = connection angle; DT = time delay.

with a relatively high background-to-peak intensity ratio, which have a very slow rising intensity profile due to large scattering effects.

5. Relation Between SEP Intensity and CME Shock Properties

We use graduated cylindrical shell (GCS) FR model (Thernisien et al., 2009; Thernisien, 2011) plus oblate spheroid shock model combined with EUV and WL data from STA, STB, SOHO, and SDO to determine 3-D structures of CME shocks (Kwon et al., 2014; Xie et al., 2017). The GCS model is used to describe the FR-like CME structure which is constrained by CME components such as three-part structure or bright frontal loops

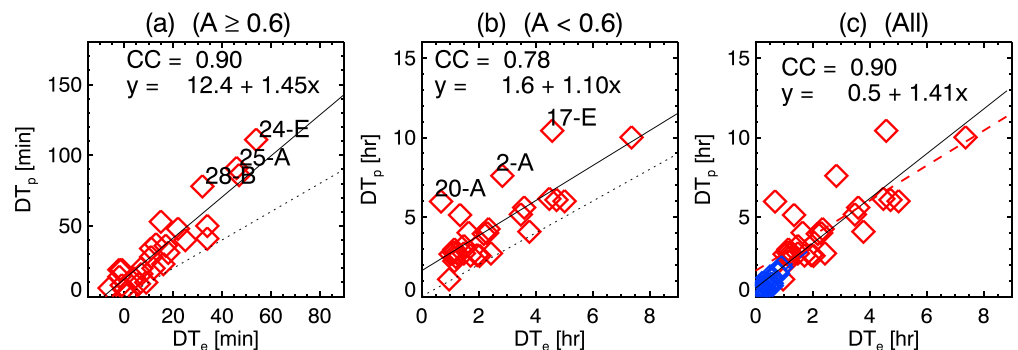


Figure 5. Comparison of electron and proton release DT s relative to Type II onset times (a) for strongly anisotropic events ($A \geq 0.6$), (b) for weakly anisotropic events ($A < 0.6$), and (c) for all the events, where blue and red diamonds denote strongly and weakly anisotropic events, respectively. The solid line is the linear fit, and the dotted line represents where DT_p is equal to DT_e . Outliers in (a) are events with $DT_p - DT_e > 13 * 3 \approx 39$ min and (b) $DT_p - DT_e > 3 * 1.5 \approx 4.5$ hr. DT = time delay.

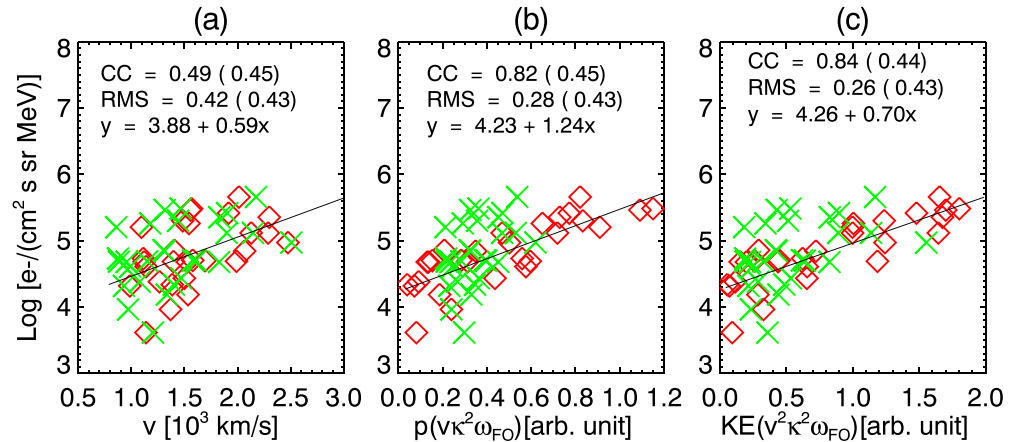


Figure 6. Correlation between logarithmic Gaussian peak intensity I_0 and true shock speed, coronal mass ejection momentum, and kinetic energy for 62- to 105-keV electrons. Red diamonds and green cross symbols denote data pairs using true shock speed v , κ , and ω_{FO} versus v_{sky} and the average values of flux rope coronal mass ejection widths, values in parentheses corresponding to green data pairs. RMS = root-mean-square.

in the WL images; the oblate spheroid is used to describe the shock front, which is constrained by EUV wave and wave-like disturbances in the WL images. We obtain the 3-D geometry shape of CME shocks and their evolution over time by fitting the GCS and shock model to near-simultaneous STEREO and SOHO WL coronagraph and STEREO and SDO EUV images of the event. The GCS model has three parameters defining the FR geometry (heliocentric height [h_{FR}], aspect ratio [κ], and half-width [α], where FR edge-on width $\omega_{EO} = 2\delta$, $\delta = \alpha \sin(\kappa)$ and FR face-on width $\omega_{FO} = 2(\alpha + \delta)$) and three parameters defining the FR orientation (longitude, latitude, and tilt angle of the FR; Thernisien et al., 2009). The oblate spheroid shock model also has six free parameters: the heights of the spheroid nose and center h and h_0 , the length of the two semiprincipal axes (a, b), and longitude and latitude of the spheroid center (see details in Xie et al., 2017). Table 1, Columns 11–13, list fit results: true shock speed $v = dh/dt$, aspect ratio κ , and half-width α . The shock speeds used in the following correlation analyses are the average linear-fit speed within the STEREO/COR2 field of view.

5.1. Correlation Between SEP Intensity and CME Shock Property

Figures 6 and 7 (from left to right) plot correlations between the Gaussian peak intensity I_0 of electrons and protons and the true shock speed v , the CME momentum $v\kappa^2\omega_{FO}$, and the CME kinetic energy $v^2\kappa^2\omega_{FO}$. Since in the GCS model, FR-CME volume is approximately equal to $Vol_{cme} = \pi\kappa^2\omega_{FO}h_{FR}^3$, the kinetic energy

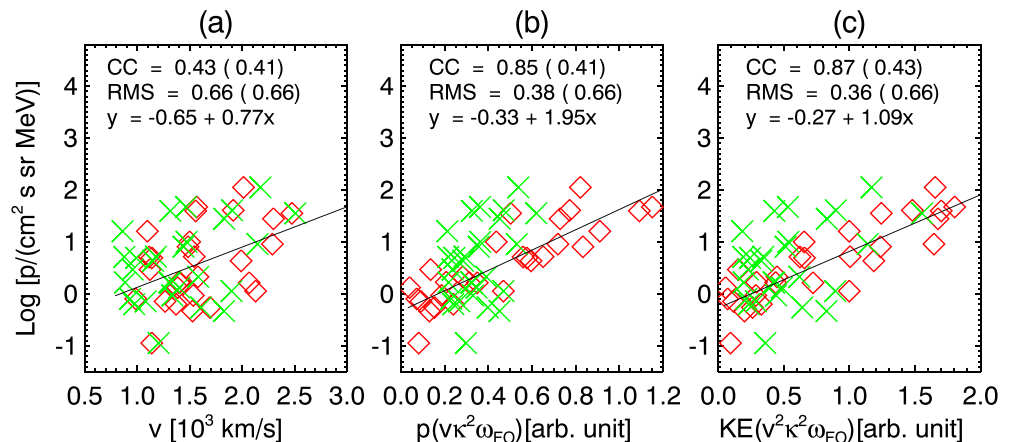


Figure 7. Correlation between logarithmic Gaussian peak intensity and true shock speed, coronal mass ejection momentum, and kinetic energy for 19- to 30-MeV protons. Red diamonds and green cross symbols denote data pairs using true shock speed v , κ , and ω_{FO} versus v_{sky} and the average values of flux rope coronal mass ejection widths, values in parentheses corresponding to green data pairs. RMS = root-mean-square.

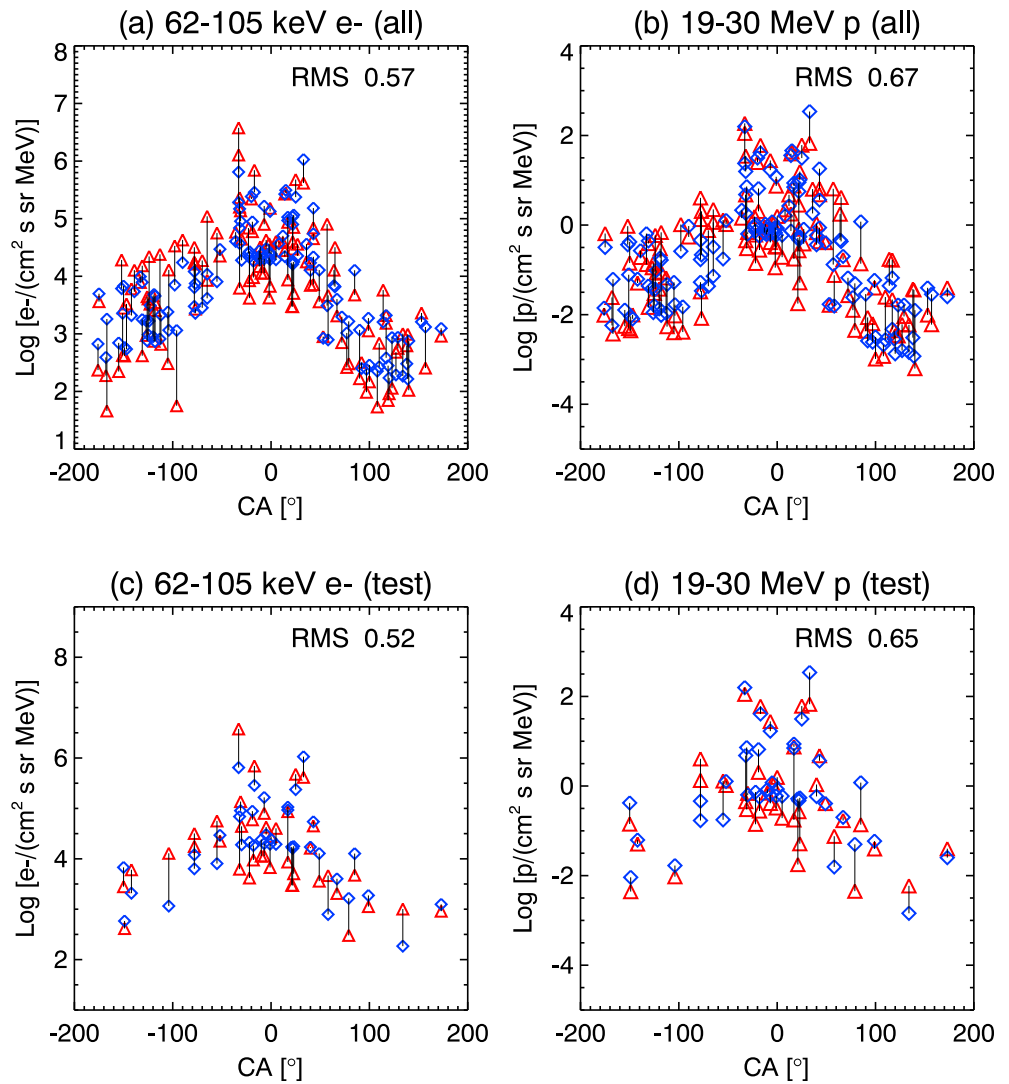


Figure 8. Comparison between predictions and observations of electron and proton intensities: (a) and (b) for training sample plus testing sample as a function of CA and (c) and (d) for testing sample only, where red triangles denote solar energetic particle observations and blue diamonds denote predicted intensities. RMS = root-mean-square; CA = connection angle.

of the CME is $(\rho \text{Vol}_{\text{cme}})v^2/2$, where ρ is the density of the FR-CME which we assume to be constant. In the analysis, we are not concerned with absolute magnitudes, so we neglect all constant factors including ρ and h_{FR} . Thus, $v\kappa^2\omega_{\text{FO}}$ and $v^2\kappa^2\omega_{\text{FO}}$ can be considered as the proxy of the CME momentum and kinetic energy.

The results show that the best correlation exists between I_0 and $v^2\kappa^2\omega_{\text{FO}}$. The correlation coefficients between I_0 and v , $v\kappa^2\omega_{\text{FO}}$, and $v^2\kappa^2\omega_{\text{FO}}$ in Figure 6 are 0.49, 0.82, and 0.84, respectively. By taking into account the CME momentum, the correlation coefficient has been improved from 0.49 to 0.81 (Figure 6b). For the case of the kinetic energy (Figure 6c), the correlation coefficient is 0.84. The root-mean-square (RMS) of the linear fit has been reduced by $\sim 38\%$ from 0.42 to 0.26 from Figures 6a to 6c. For comparison, we overplot the sky plane speed v_{sky} , $v_{\text{sky}}\kappa_{\text{avg}}^2\omega_{\text{avg}}$, and $v_{\text{sky}}^2\kappa_{\text{avg}}^2\omega_{\text{avg}}$ in the figure, marked by green cross symbols, and their correlation coefficients and RMS errors are included in parentheses. In Figure 6a, the average value of the ratio between the true shock speed and the CME sky-plane speed v/v_{sky} is 1.2. Using the true shock speed, the correlation coefficient is improved only slightly from 0.45 to 0.49, and no significant change is seen for the RMS error. In Figures 6b and 6c, since measurements of halo CME widths in the sky plane is difficult, we set ω_{FO} and κ as their average values, which is equal to 71° and 0.59, respectively. We can see that by including both the true shock speed and the true CME widths, the correlation coefficients are improved

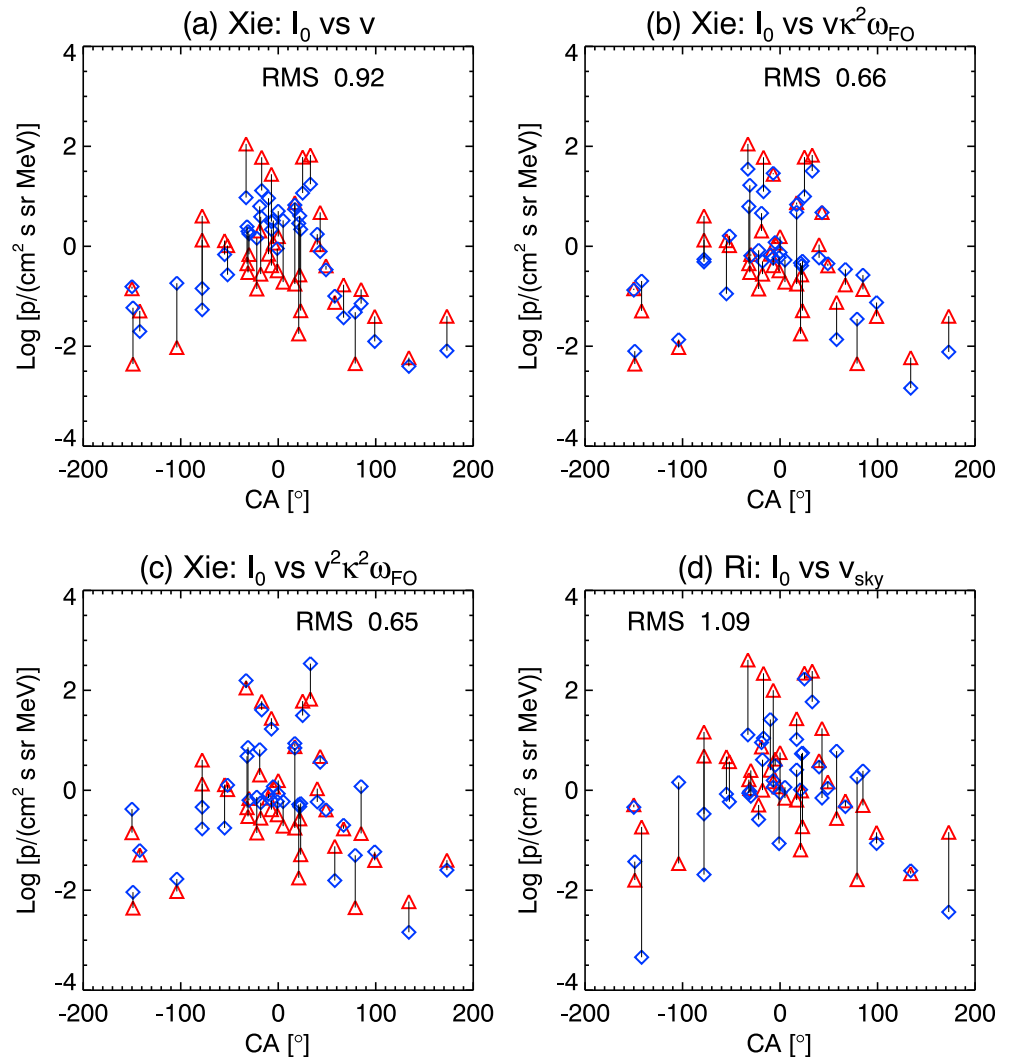


Figure 9. Comparison between predicted and observed proton intensities for the test sample using the correlations between I_0 and (a) true shock speed v , (b) $v\kappa^2\omega_{FO}$, (c) $v^2\kappa^2\omega_{FO}$ from Figure 7 in equation (3), and (d) Richardson et al.'s (2014) formula, where red triangles denote solar energetic particle observations and blue diamonds denote predicted intensities. RMS = root-mean-square; CA = connection angle.

from ~ 0.4 to ~ 0.8 by $\sim 50\%$, and the RMS errors are reduced from 0.43 to 0.28 in (Figure 6b) and to 0.26 in (Figure 6c).

Similar trend is found for proton events in Figure 7. The correlation coefficient has been improved from ~ 0.4 to ~ 0.9 from Figures 7a to 7c. The linear fit RMS error has been reduced from 0.66 to 0.36 by $\sim 45\%$. No significant improvement is seen using whether the true shock speed or the sky-plane speed in Figure 7a; however, by including the true CME widths, the correlation coefficients are improved from ~ 0.41 to ~ 0.85 in Figure 7b and from 0.43 to 0.87 in Figure 7c, and the RMS errors are reduced from 0.66 to 0.38 in Figure 7b and to 0.36 in Figure 7c. For both electrons and protons, we can see that the momentum of the CME provides a similar correlation as the CME kinetic energy. We also conducted the correlation analyses between the SEP peak intensity and ω_{FO} , κ , $v\omega_{FO}$, and $v\kappa$ and found that using a combination of $v\omega_{FO}$ and $v\kappa$ results in better correlations than using ω_{FO} and κ alone but worse than using the CME kinetic energy or momentum.

5.2. SEP Intensity Prediction as a Function of Shock Speed, CME Width, and CA

Based on correlations between Gaussian peak intensity I_0 and $v^2\kappa^2\omega_{FO}$ in Figures 6 and 7 and correlations between SEP widths σ and connection angles CA in Figure 3, we develop a formula to predict the SEP intensity observed by each spacecraft as a function of shock speed, CME width, and CA, which is given by the following.

Table 4
Observed Peak Intensities of Electrons and Protons of the Test Sample

#	Date	Type III (UT)	GCS fit		Electron intensity			Proton intensity		
			κ	α (°)	STB	e ⁻ /(cm ² s sr MeV)		p/(cm ² s sr MeV)		
						L1	STA	STB	L1	STA
1	2011/03/07	19:52	0.30	31	NA	1.60e+04	4.15e+05	NA	1.03e+00	9.46e-01
2	2011/03/21	02:21	0.81	55	NA	2.90e+03	1.01e+03	NA	2.51e-01	2.77e+01
3	2011/06/04	21:47	0.69	46	NA	NA	2.80e+03	NA	NA	6.70e+01
4	2011/06/07	06:25	0.36	12	NA	1.60e+04	NA	NA	6.07e-01	NA
5	2012/03/05	03:36	0.52	24	4.28e+04	NA	NA	1.16e+00	NA	5.92e-03
6	2012/03/07	00:18	0.64	43	4.78e+05	NA	2.77e+04	6.10e+01	NA	1.42e-01
7	2012/03/13	17:17	0.66	43	NA	1.22e+05	NA	NA	1.11e+01	NA
8	2012/03/21	07:30	0.39	18	NA	NA	NA	NA	NA	1.57e+00
9	2012/03/26	22:36	0.53	21	5.65e+04	NA	4.17e+03	1.30e+00	NA	NA
10	2012/05/26	20:46	0.35	25	4.14e+02	6.57e+03	NA	4.40e-03	1.12e-01	NA
11	2012/07/08	16:24	0.68	25	NA	1.22e+04	NA	NA	2.60e-01	NA
12	2012/07/18	05:54	0.51	28	NA	NA	3.78e+06	NA	NA	1.40e-01
13	2012/07/19	05:24	0.43	39	NA	2.30e+04	4.51e+04	NA	1.60e+00	NA
14	2012/07/23	02:14	0.66	70	NA	6.69e+03	1.76e+04	NA	2.03e-01	1.02e+03
15	2013/05/13	02:12	0.85	49	NA	1.37e+05	NA	NA	3.00e-01	NA
16	2013/05/13	16:08	0.65	32	NA	6.29e+04	NA	NA	2.03e-00	NA
17	2013/10/11	07:15	0.62	78	6.23e+03	NA	1.38e+03	4.50e-01	NA	4.77e+00
18	2013/11/02	04:28	0.84	60	6.07e+03	NA	2.99e+03	5.09e-02	NA	4.05e+00
19	2013/12/28	17:24	0.42	21	NA	5.09e+03	NA	NA	6.03e-01	1.16e-02
20	2014/02/21	15:46	0.21	32	4.03e+04	NA	NA	1.92e-01	NA	1.77e-02
21	2014/04/18	12:55	0.42	36	NA	6.23e+04	NA	NA	1.02e+00	NA
22	2014/09/01	11:03	0.66	40	6.96e+05	1.29e+03	NA	6.05e+01	5.91e-02	NA
23	2014/09/10	17:45	0.82	41	1.13e+03	3.17e+04	NA	3.96e-02	1.53e+00	NA
24	2015/06/18	01:27	0.15	8	NA	4.18e+03	NA	NA	3.97e-01	NA
25	2015/06/21	01:42	0.68	65	NA	4.50e+04	NA	NA	1.98e+00	NA
26	2015/06/25	08:16	0.27	16	NA	1.34e+04	NA	NA	4.11e-01	NA
27	2015/10/29	02:19	0.39	24	NA	9.47e+03	NA	NA	4.80e-01	NA
28	2016/01/01	23:21	0.38	7	NA	7.14e+03	NA	NA	7.63e-02	NA

Note. The peak intensities at Advanced Composition Explorer and Wind have been corrected by intercalibration factors of 1/1.4 and 1/1.5. NA = the event peak intensity has been interfered by preceding event, ion contamination, or too small to be determined; STA and STB = Solar Terrestrial Relations Observatory A and B; GCS = graduated cylindrical shell.

For electrons,

$$I(\phi) = I_0 \exp[-CA^2/2\sigma^2], \text{ where } I_0 = 10^{4.26+0.7v^2\kappa^2\omega_{FO}} \quad (3)$$

$$\sigma = \begin{cases} 7.1 + 0.26CA, & \text{if } CA \geq 0 \\ 12.9 - 0.28CA, & \text{if } CA < 0. \end{cases}$$

For protons,

$$I(\phi) = I_0 \exp[-CA^2/2\sigma^2], \text{ where } I_0 = 10^{-0.27+1.09v^2\kappa^2\omega_{FO}} \quad (4)$$

$$\sigma = \begin{cases} 8.4 + 0.21CA, & \text{if } CA \geq 0 \\ 7.9 - 0.28CA, & \text{if } CA < 0, \end{cases}$$

where (v , ω_{FO} , and CA) are in units of (10^3 km/s, 10^2 deg, and deg), respectively.

In Figure 8, it is a comparison between predictions and observations of electron (Figure 8a) and proton (Figure 8b) intensities as a function of CA . Red triangles denote SEP observations, and blue diamonds denote

predicted intensities. The test sample we use to validate the SEP prediction formula is listed in Table 4, which includes 28 SEP events selected from 2010 to 2016. Figures 8a and 8b are the comparison using both the training sample (Table 2) and test sample (Table 4) for a total of 56 events. Figures 8c and 8d are the comparison for the test sample only. We can see that the two data sets yield similar RMS errors of ~ 0.57 (0.52) for electrons and 0.67 (0.65) for protons for the whole (test) data set. In the figure where CAs range from -178° to 173° , there is consistently good agreement between observed and predicted SEP intensities at all CAs. Therefore, the prediction formula is a good estimate of SEP intensity over a wide range of CAs.

For reference, in Figure 9, we plot the comparison between observations and predictions for the protons of the test sample by replacing the three correlations from Figure 7 in equation (4) (Figures 9a–9c) and using the formula from Richardson et al. (2014; Figure 9d), which is given by $I(\phi) = I_0 \exp[-CA^2/2\sigma^2]$, $I_0 = \exp(-4.36 + 3.6v_{\text{sky}})$, where v_{sky} is the sky-plane speed of the CME in units of (10^3 km/s) and $\sigma = 43^\circ$. Since the intensity is plotted with a logarithmic scale in the figure, an RMS error of 1.0 indicates that the predicted and observed intensities differ by an order of magnitude. Note that in Richardson et al.'s (2014) study, they used 14- to 24-MeV proton data from STA/STB to match the ERNE's proton data. Compared to Richardson et al.'s (2014) prediction, we reduce the RMS error from ~ 1.1 to 0.92 in Figure 9a by using the true shock speed, and by including the true CME widths, we reduce the RMS error from ~ 1.1 to ~ 0.66 in Figure 9b and 0.65 in Figure 9c and improve the prediction by $\sim 41\%$.

6. Discussion

There are three main aspects of the results presented in this work that need further discussion.

6.1. East-West Asymmetry and σ Dependence on CA in the SEP Distribution

Previous statistical studies and transport numerical simulations have shown that the longitudinal distribution of the SEP peak intensities exhibited an east-west asymmetry. However, an asymmetry both to the east and to the west have been reported in the past. For example, Lario et al. (2013) found an asymmetry of 16° to the east for 35 STEREO 71- to 112-keV electron events. Richardson et al. (2014) reported similar results as ours in Figure 2, which had an asymmetry of 18° to the east for 62- to 105-keV electrons and of 15° to the east for 19- to 30-MeV protons. In contrast, Dresing et al. (2014) found an asymmetry of 11° to the west for 21 widespread 55- to 105-keV electron events. An asymmetric distribution of SEPs with an eastern offset was also supported in numerical simulations (e.g., Ablaßmayer et al., 2016; He & Wan, 2015; Hu et al., 2017). In He and Wan (2015, Figure 3), they plotted the simulated peak intensities of SEPs originating from different heliolongitudes with CAs ranging from -140° to 140° and showed that the peak intensities of the SEP events originating from solar sources located on the eastern side of the observer footpoint (negative CAs) are systematically larger than those of the SEP events originating from sources located on the western side (positive CAs). They suggested that this east-west asymmetry of the SEP intensity was due to the interplay among perpendicular and parallel diffusion effects and geometry of spiral magnetic field lines. Furthermore, detailed examination showed that the SEP intensity distribution cannot be fit with a single Gaussian width, and the SEP distribution width increases with the absolute value of CA. Hu et al. (2017) used a 2-D numerical model to study particle acceleration and transport at a CME-driven shock. They found that strong perpendicular diffusion is required for the observed asymmetric distribution of SEP intensities. As the perpendicular diffusion coefficient gets smaller, the SEP intensity distribution becomes nearly symmetric and more Gaussian-like. They suggested that it is the asymmetry of various shock parameters along the shock surface, such as compression ratio and obliquity, leading to the asymmetric distribution of the SEP intensity. Both He and Wan's (2015) and Hu et al.'s (2017) simulation results are consistent with our symmetric Gaussian fit results in Figure 3. In Appendix A, we show an example to discuss in detail how the east-west asymmetry causes an uncertainty in the Gaussian fit and results in varying widths and inconsistent east-west offsets reported in the past.

6.2. Relation Between Electron and Proton Release Times Relative to Type II Onset Times

Haggerty and Roelof (2009) studied the injection times of 216 near-relativistic (38–315 keV) electron events with strong beam-like anisotropies, which included 19 events associated with 50- to 100-MeV proton events; Xie et al. (2016) compared the release times of 0.25- to 10.4-MeV electrons with Type II onset times for 28 best-connected SEP events. Both studies found similar delays between the release times of near-relativistic electrons and DH Type II onset times which range from approximately -30 to 30 min. In the current study, we found that the electron release time delays for strongly anisotropic events range from approximately -25

to 54 min, where the maximum delay is larger than that obtained in the previous studies. This is because our sample includes five widespread SEP events with $|CA| > 100$, as shown in Figure 4a. We note that in the sample we study, there are 15 events associated with both metric and DH Type II bursts. The difference between the metric and DH Type II onset times range from ~ 5 to 21 min, with a mean value of ~ 15 min. There are 6 out of 28 events which are backside events with flare locations $> 50^\circ$ behind the limb. For these events, since the metric Type II radio bursts are likely occulted by the high-density plasma near the Sun, the delay between SEP particles and Type II burst onsets may be underestimated. We have tried to shift the Type II onset time 15 min earlier for the six backside events and found that four of them moved closer to the best-fit line and two of them moved away from it, implying that these two events are DH only events where the shocks might not be formed until later and higher in the corona. The correlation coefficient for delay and CA slightly increased from 0.70 to 0.73; however, the change is not significant.

One of the major reasons for the large SEP-Type II delays in the strongly anisotropic events is the poor magnetic connectivity between the flare site and the observer. This includes cases when the solar source is separated from the magnetic footpoint of the observer in either longitudinal angular distances (i.e., large CAs) or latitudinal angular distances when the Type II bursts are produced at the shock flanks while the SEPs are produced at the shock nose (e.g., Gopalswamy et al., 2014, Lario et al., 2017). By detailed examination of the 22-E event in Figure 4a on 29 September 2013, we found that its associated Type II radio burst started as a brief fragment at 21:53 UT, and continuous Type II drift did not appear until 41 min later around 22:34 UT. We speculate that the Type II fragment at 21:53 UT was likely produced at the flank in the quasi-perpendicular shock region, which was not magnetically connected to the observing spacecraft. Its SEPs were accelerated at the shock nose when the shock became stronger at later times. For the 20-B event on 21 June 2013, the electrons were released 25 min earlier than the Type II, but its protons were released 10 min after Type II. This is a small SEP event, and its associated Type II burst are ~ 40 min delayed from Type III onsets. Why the electrons were released around a half hour earlier than the Type II bursts is still not clear (cf. Cliver & Ling, 2009).

The dominating factor causing large onset delays in the weakly anisotropic events is the scattering effect. Assuming electrons are released at the same time as the Type II bursts, the onset delay observed in situ at 1 AU relative to the Type II burst onsets can be considered as the travel time of the electrons. For 62- to 105-keV electrons, the travel time along a nominal Parker spiral of 1.25-AU length is ~ 20 min (using a mean energy of 84 keV). For a mean energy of 25-MeV protons, the travel time is ~ 46 min if we assume protons are released ~ 18 min later than electrons on average (cf. section 4.2). The estimated scattering path lengths for electrons range from ~ 2.7 to 28.8 AU and for protons from ~ 2.5 to 18.0 AU. Our estimate for electrons is consistent with Dresing et al. (2014) study, where they found the scattering path lengths for 55- to 105-keV electrons up to ~ 30 AU for some extreme events. On the other hand, these large delays might also be caused by background effects due to low signal-to-noise ratios in the small intensity events, where low counting statistics and uncertainties in the instrument response may lead to apparent delay in the onset time (e.g., Lario et al., 2017; Xie et al., 2016). In addition, some proton events in the strongly anisotropic group may actually have weak anisotropy (due to lack of proton anisotropic data we used in our anisotropy analysis only electron measurements; Haggerty & Roelof, 2009). Xie et al. (2016) compared the release times of the 0.25- to 10.4-MeV electrons and 10- to 100-MeV protons for 28 best-connected SEP events. In their study, they used the velocity dispersion analysis to derive proton release times and showed that the protons were released within ~ 10 min of electron release times in most ($\sim 70\%$) of the best-connected SEP events. There were six SEP events, which had a delayed proton release time by ~ 13 –31 min with large scattering path lengths > 1.6 AU, but they were small intensity events with low signal-to-noise ratios.

6.3. Relation Between SEP Intensity and CME Shock Properties

Shock acceleration theory shows that the intensity of SEPs at a given energy is proportional to the shock strength and shock speed through the ambient medium (e.g., Lee et al., 2012). The large SEP events with intensity > 10 pfu in the GOES > 10 -MeV channel and duration exceeding a few hours are closely associated with wide and fast CMEs (Gopalswamy et al., 2005). The association between SEPs and CMEs was first pointed out by Kahler et al. (1978), leading to the idea that SEPs are accelerated by CME-driven shocks. Previous studies have found that the speed and apparent width of CMEs correlate reasonably well with the peak intensity of SEPs (Gopalswamy et al., 2002, 2004; Kahler et al., 1984; Kahler & Vourlidis, 2005; Richardson et al., 2014, 2015), as expected from the theory of the shock acceleration. The obtained correlations suggested that the CME parameters play important roles in deciding the strength of CME-driven shock. The

major problem with these correlations is that the observed scatter of points is very large, that is, the SEP intensity can vary over 3 or 4 orders of magnitude for a given CME speed and width. This is because (1) the CME speeds and widths used in the previous studies are apparent parameters measured in projection on the plane of sky and (2) halo CMEs have been excluded in the analyses due to lack of width measurements. In the current study, we replaced the apparent CME parameters with the true shock speed and CME width and found that the CME kinetic energy correlates best with the SEP peak intensity. The reduced scatter in the correlation between the CME kinetic energy and SEP intensity can not only improve the SEP intensity prediction but also provide evidence for the CME-shock acceleration theory of SEPs. However, our prediction formula based on this correlation is an empirical algorithm. Since both the Alfvén speed in the shock upstream and the CME speed relative to the upstream solar wind speed determine the shock strength, these and other factors such as seed particle population are important for the peak SEP intensities (e.g., Kahler et al., 1999; Kahler, 2001). Also, the occurrence of preceding CMEs and interacting CMEs may contribute to the scatter in the correlation between the CME speed and SEP intensity (e.g., Gopalswamy et al., 2002, 2004; Li et al., 2012). To further improve SEP intensity prediction, realistic simulations of the SEP events using observational data from near-Sun missions such as Parker Solar Probe and Solar Orbiter are necessary.

7. Summary

Using multispacecraft observations, we investigate statistically the longitudinal distribution of peak intensities, onset delays, and the relation between the Gaussian peak intensity, shock speed, CME width, and kinetic energy. Our main results are summarized below.

1. Our asymmetric Gaussian fit yields Gaussian width $\sigma = 42 \pm 7.4^\circ$ for 62- to 105-keV electrons and $\sigma = 39 \pm 6.8^\circ$ for 19- to 30-MeV protons. The average offset is $-18.3 \pm 17.0^\circ$ for electrons and $-14.6 \pm 16.1^\circ$ for protons.
2. When examining eastern and western events separately with symmetric Gaussian function, we found that Gaussian width increases with $|CA|$.
3. The average electron (proton) release time delay relative to Type II onset DT is ~ 14 (32) min for strongly anisotropic events and ~ 2.5 (4.4) hr for weakly anisotropic events. For both electrons and protons, their release time delays DT s increase with $|CA|$.
4. Poor magnetic connectivity to the flare site causing large shock lateral traveling time in strongly anisotropic events and scattering effects in weakly anisotropic events are two major reasons for the large SEP onset delays relative to Type II onset times.
5. The best correlation exists between the Gaussian peak intensity I_0 and the proxy CME kinetic energy $v^2 \kappa^2 \omega_{FO}$, where $\kappa^2 \omega_{FO}$ is proportional to the FR CME widths. By taking into account the effects of FR CME widths, the correlation coefficients in Figure 6 can be improved from ~ 0.5 to 0.8 for electrons and ~ 0.4 to 0.9 for protons in Figure 7. Compared to Richardson et al.'s (2014) prediction, we reduce the RMS error on the predicted SEP intensity by $\sim 41\%$ for protons. The improved correlation between the CME kinetic energy and SEP intensity provides strong evidence for the CME-shock acceleration theory of SEPs.

Appendix A: Uncertainties From the Gaussian Fit

It is common to fit the peak intensities observed from multiple spacecraft with Gaussian function to investigate the longitudinal distribution of SEPs. However, how we determine the peak intensity of SEPs may affect the fit results. Figure A1a shows electron intensity observations from STA, STB, and ACE during the 5 March 2013 SEP event. The intensity on the best-connected STA ($CA = 14$) reached the maximum value at 10:08 UT on 5 March. The intensities on STB with $CA = -90$ and ACE with $CA = 157$, however, increase monotonically with time, which result in a varying peak intensity depending on the selected time profile durations. This varying peak intensity would therefore affect the width of Gaussian fit and add an uncertainty in the Gaussian fit. As shown in the figure, the western event on ACE (green) tended to increase initially and reach a plateau gradually, while the eastern event on STB (blue) increased faster until the intensity peaking at the passage of the associated IP shock. In Figure A1b, we plot the fit results using peak intensities from durations of 6, 24, and 48 hr. The fit yields an eastern width σ_{east} of 27° , 32° , and 45° on STB, respectively, and western width σ_{west} of 39° , 40° , and 42° on ACE. The uncertainty in the Gaussian fit due to selecting different

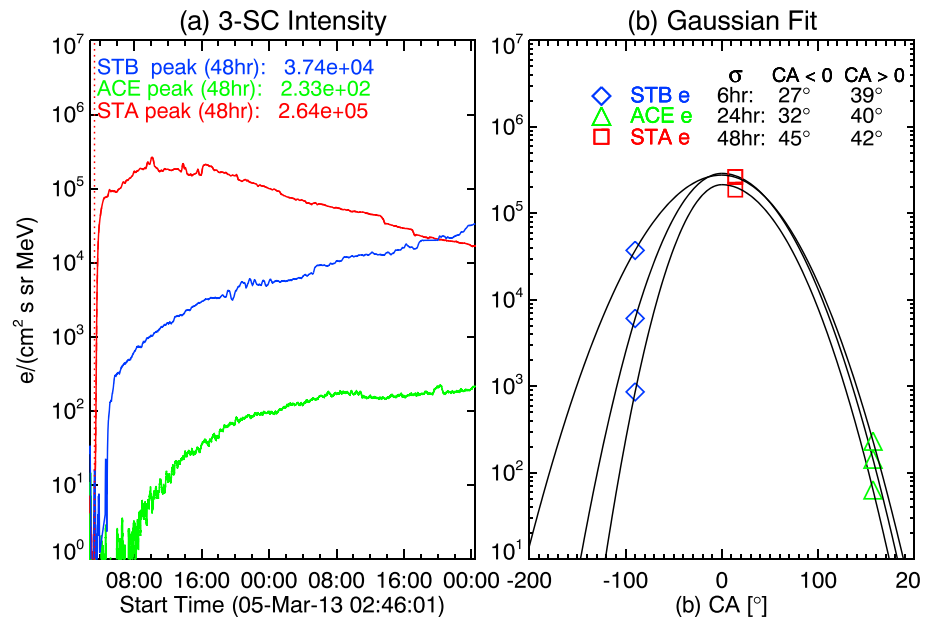


Figure A1. (a) Intensity time profiles of 62- to 105-keV electrons on 5 March 2013 observed by STA (red), STB (blue), and ACE (green) and (b) symmetric Gaussian fit results of the event using peak intensities from time durations of 6, 24, and 48 hr, respectively. STA and STB = Solar Terrestrial Relations Observatory A and B; ACE = Advanced Composition Explorer.

durations results in varying widths and inconsistent offsets. The fit results from the three durations yield an east-west asymmetry offset $\sigma_{\text{west}} - \sigma_{\text{east}}$ of 12° , 8° , and -3° , where positive and negative offsets represent an asymmetry to west and east, respectively.

Acknowledgments

The authors would like to thank the support of STEREO, SOHO, WIND, and ACE teams. The STEREO SECCHI data are produced by a consortium of RAL (UK), NRL (USA), LMSAL (USA), GSFC (USA), MPS (Germany), CSL (Belgium), IOTA (France), and IAS (France). The SOHO LASCO data are produced by a consortium of the Naval Research Laboratory (USA), Max-Planck-Institut für Aeronomie (Germany), Laboratoire d'Astronomie (France), and the University of Birmingham (UK). STEREO High Energy Telescope (HET) data were obtained online (<http://www.srl.caltech.edu/STEREO/Public/HET&urlscore:public.html>), STEREO High Energy Telescope (LET) data were obtained online (<http://www.srl.caltech.edu/STEREO/Public/LET&urlscore:public.html>), STEREO Solar Electron Proton Telescope data (SEPT) were obtained online (<http://www2.physik.uni-kiel.de/STEREO/index.php?doc=data>), and Wind/EPACT and ACE/EPAM proton and electron data were obtained online (<http://cdaweb.gsfc.nasa.gov/istp&urlscore:public/>). This work was supported by NASA LWS TR&T program NNX15AB70G. P. M. was partially supported by NASA Grant NNX15AB77G and NSF Grant AGS-1358274.

References

- Ablaßmayer, J., Tautz, R. C., & Dresing, N. (2016). Transport of solar electrons in the turbulent interplanetary magnetic field. *Physics of Plasmas*, 23(1), 12901. <https://doi.org/10.1063/1.4939023>
- Bougeret, J. L., Goetz, K., Kaiser, M. L., Bale, S. D., Kellogg, P. J., Maksimovic, M., & Zouganelis, I. (2008). S/WAVES: The radio and plasma wave investigation on the STEREO mission. *Space Science Reviews*, 136, 487–528. <https://doi.org/10.1007/s11214-007-9298-8>
- Bougeret, J. L., Kaiser, M. L., Kellogg, P. J., Manning, R., Goetz, K., Monson, S. J., & Hoang, S. (1995). Waves: The radio and plasma wave investigation on the Wind spacecraft. *Space Science Reviews*, 71, 231–263. <https://doi.org/10.1007/BF00751331>
- Cliver, E. W., Kahler, S. W., Neidig, D. F., Cane, H. V., Richardson, I. G., Kallenrode, M. B., & Wibberenz, G. (1995). Extreme “propagation” of solar energetic particles. *International Cosmic Ray Conference*, 4, 257.
- Cliver, E. W., & Ling, A. G. (2009). Low-frequency type III bursts and solar energetic particle events. *The Astrophysical Journal*, 690, 598–609. <https://doi.org/10.1088/0004-637X/690/1/598>
- Dresing, N., Gómez-Herrero, R., Heber, B., Klassen, A., Malandraki, O., Dröge, W., & Kartavykh, Y. (2014). Statistical survey of widely spread out solar electron events observed with STEREO and ACE with special attention to anisotropies. *Astronomy & Astrophysics*, 567, A27. <https://doi.org/10.1051/0004-6361/201423789>
- Gold, R. E., Krimigis, S. M., Hawkins, S. E. III., Haggerty, D. K., Lohr, D. A., Fiore, E., & Lanzerotti, L. J. (1998). Electron, proton, and alpha monitor on the Advanced Composition Explorer spacecraft. *Space Science Reviews*, 86, 541–562. <https://doi.org/10.1023/A:1005088115759>
- Gopalswamy, N., Xie, H., Akiyama, S., Mäkelä, P. A., & Yashiro, S. (2014). Major solar eruptions and high-energy particle events during solar cycle 24. *Earth, Planets, and Space*, 66, 104. <https://doi.org/10.1186/1880-5981-66-104>
- Gopalswamy, N., Yashiro, S., Krucker, S., & Howard, R. A. (2005). CME interaction and the intensity of solar energetic particle events. In K. Dere, J. Wang, & Y. Yan (Eds.), *Astronomical Union 226, Held 13-17 September, Beijing* (pp. 367–373). Cambridge: Cambridge University Press. <https://doi.org/10.1017/S1743921305000876>
- Gopalswamy, N., Yashiro, S., Krucker, S., Stenborg, G., & Howard, R. A. (2004). Intensity variation of large solar energetic particle events associated with coronal mass ejections. *Journal of Geophysical Research*, 109, A12105. <https://doi.org/10.1029/2004JA010602>
- Gopalswamy, N., Yashiro, S., Michalek, G., Kaiser, M. L., Howard, R. A., Reames, D. V., & von Rosenvinge, T. (2002). Interacting coronal mass ejections and solar energetic particles. *The Astrophysical Journal Letters*, 572, L103–L107. <https://doi.org/10.1086/341601>
- Haggerty, D. K., & Roelof, E. C. (2009). Probing SEP acceleration processes with near-relativistic electrons. In X. Ao & G. Z. R. Burrows (Eds.), *18th Annual International Astrophysics Conference, Held 1-7 May, Kona Hawaii, American institute of physics conference series* (Vol. 1183, pp. 3–10). <https://doi.org/10.1063/1.3266783>
- He, H. Q., & Wan, W. (2015). Numerical study of the longitudinally asymmetric distribution of solar energetic particles in the heliosphere. *The Astrophysical Journal Supplement Series*, 218, 17. <https://doi.org/10.1088/0067-0049/218/2/17>
- Howard, R. A., Moses, J. D., Vourlidas, A., Newmark, J. S., Socker, D. G., Plunkett, S. P., & Carter, T. (2008). Sun Earth Connection Coronal and Heliospheric Investigation (SECCHI). *Space Science Reviews*, 136, 67–115. <https://doi.org/10.1007/s11214-008-9341-4>

- Hu, J., Li, G., Ao, X., Zank, G. P., & Verkhoglyadova, O. (2017). Modeling particle acceleration and transport at a 2-D CME-driven shock. *Journal of Geophysical Research: Space Physics*, *122*, 10,938–10,963. <https://doi.org/10.1002/2017JA024077>
- Kahler, S. W. (2001). The correlation between solar energetic particle peak intensities and speeds of coronal mass ejections: Effects of ambient particle intensities and energy spectra. *Journal of Geophysical Research*, *106*(A10), 20,947–20,955. <https://doi.org/10.1029/2000JA002231>
- Kahler, S., Burkepile, J., & Reames, D. (1999). Coronal/interplanetary factors contributing to the intensities of E > 20 MeV gradual solar energetic particle events. *International Cosmic Ray Conference*, *6*, 248.
- Kahler, S. W., Hildner, E., & Van Hollebeke, M. A. I. (1978). Prompt solar proton events and coronal mass ejections. *Solar Physics*, *57*(2), 429–443. <https://doi.org/10.1007/BF00160116>
- Kahler, S. W., Sheeley, N. R., Howard, R. A., Michels, D. J., Koomen, M. J., McGuire, R. E., & Reames, D. V. (1984). Associations between coronal mass ejections and solar energetic proton events. *Journal of Geophysical Research*, *89*, 9683–9693. <https://doi.org/10.1029/JA089iA11p09683>
- Kahler, S. W., & Vourlidas, A. (2005). Fast coronal mass ejection environments and the production of solar energetic particle events. *Journal of Geophysical Research*, *110*, A12S01. <https://doi.org/10.1029/2005JA011073>
- Kaiser, M. L., Kucera, T. A., Davila, J. M., Cyr, O. C. S., Guhathakurta, M., & Christian, E. (2008). The STEREO mission: An introduction. *Space Science Reviews*, *136*, 5–16.
- Klein, K. L., Krucker, S., Lointier, G., & Kerdran, A. (2008). Open magnetic flux tubes in the corona and the transport of solar energetic particles. *Astronomy & Astrophysics*, *486*, 589–596. <https://doi.org/10.1051/0004-6361/20079228>
- Kwon, R. Y., Zhang, J., & Olmedo, O. (2014). New insights into the physical nature of coronal mass ejections and associated shock waves within the framework of the three-dimensional structure. *The Astrophysical Journal*, *794*, 148. <https://doi.org/10.1088/0004-637X/794/2/148>
- Lario, D., Aran, A., Gómez-Herrero, R., Dresing, N., Heber, B., Ho, G. C., & Roelof, E. C. (2013). Longitudinal and radial dependence of solar energetic particle peak intensities: STEREO, ACE, SOHO, GOES, and MESSENGER observations. *The Astrophysical Journal*, *767*, 41. <https://doi.org/10.1088/0004-637X/767/1/41>
- Lario, D., Kwon, R. Y., Richardson, I. G., Raouafi, N. E., Thompson, B. J., von Rosenvinge, T. T., & Riley, P. (2017). The solar energetic particle event of 2010 August 14: Connectivity with the solar source inferred from multiple spacecraft observations and modeling. *The Astrophysical Journal*, *838*, 51. <https://doi.org/10.3847/1538-4357/aa63e4>
- Lee, M. A., Mewaldt, R. A., & Giacalone, J. (2012). Shock acceleration of ions in the heliosphere. *Space Science Reviews*, *173*(1-4), 247–281. <https://doi.org/10.1007/s11214-012-9932-y>
- Lemen, J. R., Title, A. M., Akin, D. J., Boerner, P. F., Chou, C., Drake, J. F., & Waltham, N. (2012). The Atmospheric Imaging Assembly (AIA) on the Solar Dynamics Observatory (SDO). *Solar Physics*, *275*, 17–40. <https://doi.org/10.1007/s11207-011-9776-8>
- Leske, R. A., Cohen, C. M. S., Mewaldt, R. A., Christian, E. R., Cummings, A. C., Labrador, A. W., & von Rosenvinge, T. T. (2012). Large proton anisotropies in the 18 August 2010 solar particle event. *Space Science Reviews*, *281*, 301–318. <https://doi.org/10.1007/s11207-012-0018-5>
- Li, G., Moore, R., Mewaldt, R. A., Zhao, L., & Labrador, A. W. (2012). A twin-CME scenario for ground level enhancement events. *Space Science Reviews*, *171*(1-4), 141–160. <https://doi.org/10.1007/s11214-011-9823-7>
- Müller-Mellin, R., Böttcher, S., Falenski, J., Rode, E., Duvert, L., Sanderson, T., & Smit, H. (2008). The solar electron and proton telescope for the STEREO Mission. *Space Science Reviews*, *136*, 363–389. <https://doi.org/10.1007/s11214-007-9204-4>
- Richardson, I. G., Cane, H. V., & von Rosenvinge, T. T. (1991). Prompt arrival of solar energetic particles from far eastern events—The role of large-scale interplanetary magnetic field structure. *Space Physics*, *96*, 7853–7860. <https://doi.org/10.1029/91JA00379>
- Richardson, I. G., von Rosenvinge, T. T., & Cane, H. V. (2015). The properties of solar energetic particle event-associated coronal mass ejections reported in different CME catalogs. *Solar Physics*, *290*, 1741–1759. <https://doi.org/10.1007/s11207-015-0701-4>
- Richardson, I. G., von Rosenvinge, T. T., Cane, H. V., Christian, E. R., Cohen, C. M. S., Labrador, A. W., & Stone, E. C. (2014). > 25 MeV proton events observed by the high energy telescopes on the STEREO A and B spacecraft and/or at Earth during the first seven years of the STEREO mission. *Solar Physics*, *289*, 3059–3107. <https://doi.org/10.1007/s11207-014-0524-8>
- Rouillard, A. P., Sheeley, N. R., Tylka, A., Vourlidas, A., Ng, C. K., Rakowski, C., & Szabo, A. (2012). The longitudinal properties of a solar energetic particle event investigated using modern solar imaging. *The Astrophysical Journal*, *752*, 44. <https://doi.org/10.1088/0004-637X/752/1/44>
- Schrijver, C. J., Title, A. M., Yeates, A. R., & DeRosa, M. L. (2013). Pathways of large-scale magnetic couplings between solar coronal events. *The Astrophysical Journal*, *773*, 93. <https://doi.org/10.1088/0004-637X/773/2/93>
- Thernisien, A. (2011). Implementation of the graduated cylindrical shell model for the three-dimensional reconstruction of coronal mass ejections. *The Astrophysical Journal Supplement*, *194*, 33. <https://doi.org/10.1088/0067-0049/194/2/33>
- Thernisien, A., Vourlidas, A., & Howard, R. A. (2009). Forward modeling of coronal mass ejections using STEREO/SECCHI data. *Solar Physics*, *256*, 111–130. <https://doi.org/10.1007/s11207-009-9346-5>
- Torsti, J., Valtonen, E., Lumme, M., Peltonen, P., Eronen, T., Louhola, M., & Strömmer, E. (1995). Energetic particle experiment ERNE. *Solar Physics*, *162*, 505–531. <https://doi.org/10.1007/BF00733438>
- von Rosenvinge, T. T., Reames, D. V., Baker, R., Hawk, J., Nolan, J. T., Ryan, L., & Wiedenbeck, M. E. (2008). The high energy telescope for STEREO. *Space Science Reviews*, *136*, 391–435. <https://doi.org/10.1007/s11214-007-9300-5>
- Wiedenbeck, M. E., Mason, G. M., Cohen, C. M. S., Nitta, N. V., Gómez-Herrero, R., & Haggerty, D. K. (2013). Observations of solar energetic particles from ³He-rich events over a wide range of heliographic longitude. *The Astrophysical Journal*, *762*, 54. <https://doi.org/10.1088/0004-637X/762/1/54>
- Wueller, J. P., Lemen, J. R., Tarbell, T. D., Wolfson, C. J., Cannon, J. C., Carpenter, B. A., & Deutsch, W. (2004). EUVI: The STEREO-SECCHI extreme ultraviolet imager. In S. Fineschi & M. A. Gummin (Eds.), *Telescopes and Instrumentation for Solar Astrophysics, Proceedings of the SPIE* (5171, pp. 111–122). <https://doi.org/10.1117/12.506877>
- Xie, H., Mäkelä, P., Gopalswamy, N., & St. Cyr, O. C. (2016). Energy dependence of SEP electron and proton onset times. *Journal of Geophysical Research: Space Physics*, *121*, 6168–6183. <https://doi.org/10.1002/2015JA021422>
- Xie, H., Mäkelä, P., St. Cyr, O. C., & Gopalswamy, N. (2017). Comparison of the coronal mass ejection shock acceleration of three widespread SEP events during solar cycle 24. *Journal of Geophysical Research: Space Physics*, *122*, 7021–7041. <https://doi.org/10.1002/2017JA024218>
- Yashiro, S., Gopalswamy, N., Michalek, G., St. Cyr, O. C., Plunkett, S. P., Rich, N. B., & Howard, R. A. (2004). A catalog of white light coronal mass ejections observed by the SOHO spacecraft. *Journal of Geophysical Research*, *109*, A07105. <https://doi.org/10.1029/2003JA010282>
- Zhang, M., Qin, G., & Rassoul, H. (2009). Propagation of solar energetic particles in three-dimensional interplanetary magnetic fields. *The Astrophysical Journal*, *692*, 109–132. <https://doi.org/10.1088/0004-637X/692/1/109>

Zhang, M., & Zhao, L. (2017). Precipitation and release of solar energetic particles from the solar coronal magnetic field. *The Astrophysical Journal*, 846, 107. <https://doi.org/10.3847/1538-4357/aa86a8>